Loop energy : A useful indicator of the hardness of minerals from depth-sensing indentation tests

Loop energy: a useful indicator of the hardness of minerals from depth-sensing indentation tests

Toshiaki Masuda,[1,2,*] Yasutomo Omori,[1,2] Ryoko Sakurai,[1] Tomoya Miyake,[1] Mirai Yamanouchi,[1] Yumiko Harigane,[1,3] Atsushi Okamoto,[1,4] and Katsuyoshi Michibayashi[1,5]

[1]Institute of Geosciences, Shizuoka University, Ohya 836, Suruga-ku, Shizuoka 422-8529, Japan

[2]Center for Integrated Research and Education of Natural Hazards, Shizuoka University, Ohya 836, Suruga-ku, Shizuoka 422-8529, Japan

[3]Geological Survey of Japan, AIST, Umezono 1-1-1, Tsukuba 305-8567, Japan

[4]Graduate School of Environmental Studies, Tohoku University, Aramaki 468-1, Aoba-ku, Sendai 980-8579, Japan

[5]Department of Earth Sciences, Nagoya University, Chikusa, Nagoya City, Aichi, 446, Japan

*Corresponding author

E-mail: masuda.toshiaki@shizuoka.ac.jp

Tel: +81-54-238-4785

Postal address: Center for Integrated Research and Education of Natural Hazards, Shizuoka University, Ohya 836, Suruga-ku, Shizuoka 422-8529, Japan

Key-words: Depth-sensing indentation test; Loop energy; Mohs hardness scale; New graphic presentation; Penetration depth.

'Declarations of interest: none'

Abstract

Depth-sensing indentation tests were performed to obtain the loop energy (equivalent to the energy consumed to produce the indentation) and the residual depth of the indentation using a triangular pyramidal diamond indenter for the minerals in Mohs hardness scale except for diamond, as well as other minerals (apophyllite, forsterite, and tourmaline), at a maximum load ranging from 30 to 100 mN. A new graphic presentation is proposed that shows the hardness of minerals in log(penetration depth)–log(loop energy) space. The data for each mineral under different loads give a straight regression line with a slope of 2.6–2.9 (except for talc, which yields a slope of 2.2), while the data for different minerals under a given load yield a straight regression line with a slope of 1.1–1.2. A theoretical analysis of ideal materials, in terms of log(penetration depth)–log(loop energy) space, shows the existence of two series of parallel regression lines with slopes of 3 (data for each mineral at different loads) and 1 (data for different minerals under a given load). The results show a slight deviation between the measured and theoretical slopes, probably reflecting a progressive change in the mechanical properties of the minerals during the indentation tests.

1. Introduction

Indentation testing has been employed for more than 100 years as a practical method for measuring the hardness of solids (e.g., Tabor, 1996; Walley, 2012). The method has two advantages: (1) sample preparation is simple compared with other mechanical tests, because only a small area of specimen is required; and (2) indentation testers are sufficiently compact to be used on a small table top and are easy to operate. A range of indices (e.g., the Vickers, Brinell, Knoop, Rockwell, Meyer and Martel hardnesses) have been proposed for various purposes (e.g., Knoop *et al*., 1939; Tabor, 1951; Mott, 1956; Westbrook & Conrad, 1973; Szymański & Szymański, 1989; Fischer-Cripps, 2004; Milman et al., 2014). The hardness of minerals has been measured by indentation tests under room conditions (e.g., Hodge & McKay, 1934; Winchell, 1945; Tabor, 1954; Brace, 1963, 1964; Ferguson *et al*., 1987; Karato et al., 1990; Li & Bradt, 1990, 1991; Dhar *et al*., 1997; Masuda *et al*., 2000; Golsby *et al*., 2004; Broz *et al*., 2006; Whitney *et al*., 2007, and references therein) and at high temperatures (e.g., Westbrook, 1958; Evans &Goetze, 1979; Evans, 1984; Darot *et al*., 1985; Karato *et al*., 1986; Dorner &Stöckhert, 2004).

The widely used classical testers employ a dead-weight-type loading system. The user selects the weight of the pyramidal indenter before the test and can only measure the size of the produced indentation after the test. In the 1970s, technological innovations enabled the development of depth-sensing indentation testers, and these have become increasingly popular (e.g., Grigorovich, 1976; Pethica *et al*., 1983; Doerner & Nix, 1986; Oliver & Pharr, 1992; Sakai *et al*., 1999; Fischer-Cripps, 2004; Broz *et al*., 2006; Whitney *et al*., 2007, and references therein). These testers enable the simultaneous measurement of load and displacement (penetration depth) with high precision during the indentation test, and have spurred further progress in measurements of fracture toughness, and the plasticity and elasticity of materials (e.g., Oliver & Pharr, 1992; Broz *et al*., 2006; Whitney *et al*., 2007, and references therein). The use of such testers enables the evaluation of physically meaningful parameters such as the energy required to create the indentation and creep data for earthquake mechanics (e.g., Sakai *et al*., 1993; Nowak & Sakai, 1994; Fischer-Cripps, 2004; Goldsby *et*

al., 2004). However, most of the recent hardness studies employing depth-sensing indentation testers continue to use classical hardness indices (e.g., Broz *et al*., 2006; Whitney *et al*., 2007), even though this approach does not take full advantage of the advanced technology of modern testers. In the present study, we aim to increase the utility of the energy required to make an indentation as a new indicator of the hardness of minerals, and propose a new graphic presentation that portrays the relation between the energy and the residual depth of the indentation for typical rock-forming minerals, including the minerals of Mohs hardness scale except for diamond.

2. Theoretical analysis

2.1. Basic equations

In terms of theoretical analysis we are concerned with the load applied to the specimen (y) by the pyramidal shaped indenter and the penetration depth of the indenter from the flat surface of the test specimen (x). Figure 1 shows a schematic of the power-law relation between load (y) and depth (x) during loading, expressed by

$$y = k_1 x^m, \qquad (1)$$

and the relation during unloading, expressed by

$$y = k_2 \left(x - D_r \right)^m, \qquad (2)$$

where k_1 and k_2 are constants related to the tested material, D_r is the depth of the indentation in the test specimen after complete unloading, and m is the loading and unloading exponent (e.g., Oliver & Pharr, 1992). The value of m is assumed to be the same

for the loading and unloading stages as a first approximation. Boundary conditions are given for both curves as follows:

‘insert Fig. 1 here’

$$P_{\max} = k_1 \left(D_{\max} \right)^m \qquad (3)$$

and

$$P_{\max} = k_2 \left(D_{\max} - D_r \right)^m, \qquad (4)$$

where $P_{\max}$ and $D_{\max}$ are the maximum load and corresponding maximum depth, respectively. From equations (3) and (4), we respectively derive the following equations:

$$D_{\max} = \left(\frac{P_{\max}}{k_1} \right)^{1/m} \qquad (5)$$

and

$$D_{\max} - D_r = \left(\frac{P_{\max}}{k_2} \right)^{1/m} . \qquad (6)$$

We introduce loop energy in this analysis. Loop energy was first proposed by Sakai (1993) as the energy consumed to produce indentations. The loop energy (U_r) required to produce indentation U_r is equivalent to the area outlined by the loading and unloading curves (shaded area in Fig. 1), and is calculated by

$$U_r = \int_0^{D_{\max}} k_1 x^m \, dx - \int_{D_r}^{D_{\max}} k_2 \left(x - D_r\right)^m dx = \frac{k_1}{m+1}\left(D_{\max}\right)^{m+1} - \frac{k_2}{m+1}\left(D_{\max} - D_r\right)^{m+1}. \quad (7)$$

Using equations (5) and (6), we can eliminate $D_{\max}$ from equation (7) as follows:

$$U_r = \frac{k_1}{m+1}\left(\frac{P_{\max}}{k_1}\right)^{(m+1)/m} - \frac{k_2}{m+1}\left(\frac{P_{\max}}{k_2}\right)^{(m+1)/m} = \frac{1}{m+1}\left[\left(\frac{1}{k_1}\right)^{1/m} - \left(\frac{1}{k_2}\right)^{1/m}\right]\left(P_{\max}\right)^{(m+1)/m}. \quad (8)$$

To simplify these equations, a new parameter k_0 is defined as follows:

$$\left(\frac{1}{k_0}\right)^{1/m} = \left(\frac{1}{k_1}\right)^{1/m} - \left(\frac{1}{k_2}\right)^{1/m}. \quad (9)$$

Introducing k_0, equation (8) becomes

$$U_r = \frac{1}{m+1}\left(\frac{1}{k_0}\right)^{1/m}\left(P_{\max}\right)^{(m+1)/m}. \quad (10)$$

Eliminating $D_{\max}$ from equations (5) and (6) gives

$$D_r = \left[\left(\frac{1}{k_1}\right)^{1/m} - \left(\frac{1}{k_2}\right)^{1/m}\right]\left(P_{\max}\right)^{1/m}. \quad (11)$$

Substituting k_0 into equation (11) affords

$$D_r = \left(\frac{P_{\max}}{k_0}\right)^{1/m}, \quad (12)$$

which is equivalent to

$$P_{\max} = k_0 \left(D_r \right)^m . \qquad (13)$$

Then, using equation (12), equation (10) can be rewritten as

$$U_r = \frac{1}{m+1} D_r \times P_{\max} . \qquad (14)$$

Similarly, substituting equation (13) into (14), we have

$$U_r = \frac{1}{m+1} k_0 \left(D_r \right)^{m+1} . \qquad (15)$$

2.1. Ideal load–displacement curve

Previous analyses of load and displacement data during depth-sensing indentation tests have demonstrated the quadratic relation between applied load and displacement ($m = 2$) (Sakai, 1993, 1999; Cook & Pharr, 1994; Sakai *et al*., 1999). Based on a dimensional analysis, Cheng & Cheng (1998a, b) also revealed that the relation between load and displacement for a conical indenter is quadratic. In this context, $m = 2$ appears ideal for a pyramidal indenter.

If we accept $m = 2$, then from equations (14) and (15) we have

$$y = k_1 x^2 \qquad (18)$$

and

$$y = k_2\left(x - D_r^*\right)^2. \qquad (19)$$

We similarly and consequently obtain the following two simple equations by substituting $m = 2$ into equations (14) and (15):

$$U_r^* = \frac{1}{3} D_r^* \times P_{\max} \qquad (20)$$

and

$$U_r^* = \frac{1}{3} k_0 \left(D_r^*\right)^3, \qquad (21)$$

respectively. In these equations, an asterisk (*) indicates the ideal quadratic relation in theory (in fact, $m \neq 2$ for minerals, as shown below).

2.3. Dual parallel regression lines in log D_r–log U_r space for ideal data

Equations (20) and (21) provide the theoretical basis for dual parallel regression lines in log D_r–log U_r space. Equation (20) states that U_r^* is proportional to D_r^* if $P_{\max}$ is constant. This means that the iso-load lines for different imaginary minerals are expected to be straight, and the slope of the line in log D_r–log U_r space is 1. Equation (21) demonstrates that U_r^* is proportional to $\left(D_r^*\right)^3$ if k_0 is constant. The value of k_0 is regarded as a material constant that is unique to each mineral. Thus, the data points of each imaginary mineral at different loads plotted in log D_r–log U_r space should lie on a single straight line with a slope of 3.

3. Depth-sensing indentation tests

3.1. Data of indentation tests

Figure 2 shows the schematic loading–unloading cycle for a depth-sensing indentation test, consisting of loading, dwelling, and unloading curves, corresponding to the loading, dwelling and unloading stages of the test, respectively (e.g., Pethica *et al*., 1983; Doerner & Nix, 1986; Oliver & Pharr, 1992; Sakai *et al*., 1999; Fischer-Cripps, 2004, and references therein). The term $P_{\max}$ is the maximum load, D_1 is the measured displacement at $P_{\max}$, and Δx is the displacement during the dwelling time at $P_{\max}$, which is not considered in the theoretical analysis (Fig. 1). In a typical indentation test, Δx cannot be zero due to instrumental reasons and is defined as D_2 - D_1, where D_2 is the maximum displacement during the test. The term D_3 is the displacement after complete unloading, given by the intersection of the unloading curve with the displacement axis. The term U_3 is the loop energy corresponding to the residual depth of D_3. One can assign $P_{\max}$ and the loading, dwelling, and unloading times before the test starts. The measured displacement during the actual indentation test is not equal to the penetration depth of the indenter, as during loading and unloading the test system (i.e., the frame of the tester, the indenter shaft, and the specimen mounting) is elastically deformed (e.g., Fischer-Cripps, 2006). Thus, the tester reads the sum of the real penetration depth of the indenter into the specimen plus the elastic deformation of the test system. Unfortunately, we have not yet evaluated the deformation of the test system used in this study. However, despite the unknown elastic deformation of the tester, D_3 and U_3 are considered independent of the influence of elastic deformation of the tester during the indentation test, because the loading and unloading curves are equally affected by the elastic deformation. Note that Δx in Fig. 2 is also unaffected by elastic deformation of the tester.

‘insert Fig. 2 here’

3.2. Derivation of D_r and U_r from measured data

Although D_r and U_r are key data in the theoretical analysis, we are unable to directly obtain these values during the indentation test; however, they can be calculated from the measured data as follows:

$$D_r = D_3 - \Delta x. \qquad (16)$$

and

$$U_r = U_3 - P_{\max} \cdot \Delta x. \qquad (17)$$

Figure 2 helps to understand equations (16) and (17). The values of D_r and U_r are not affected by elastic deformation of the tester because the measured data (D_3, U_3 and Δx) are independent of any elastic deformation.

3.3. Specimens

The minerals in Mohs hardness scale, except for diamond (i.e., talc, gypsum, calcite, fluorite, apatite, orthoclase, quartz, topaz, and corundum), and three other minerals (tourmaline, forsterite, and apophyllite) were used for the indentation tests. The properties of the mineral specimens are listed in Table 1, and photographs of the specimens are provided in Fig. 3. The talc and apatite specimens are polycrystalline but the others are single crystals. The indented surfaces of the quartz and calcite specimens are both oriented perpendicular to the c-axis, but the crystallographic orientations of the other crystalline mineral specimens are unknown. The mineral specimens, purchased from gem dealers in Japan, Pakistan, and the USA, were cut with a low-speed saw (ISOMET, Buhler Co., Germany) and polished using an alumina suspension (60 nm) for 6 hours to obtain an extraordinarily flat surface for the indentation tests.

‘insert Fig. 3 and Table 1 here’

3.4. Indentation tester and test procedure

The depth-sensing indentation tests were performed using a RIDER II device (Mitsutoyo Co., Japan) at Shizuoka University, Japan, equipped with a triangular pyramidal diamond indenter (face angle = 68°). The RIDER II simultaneously measures the applied load and displacement 10 times per second with a precision of 0.02 mN and 0.1 nm, respectively.

The maximum load of the tests ($P_{\max}$) ranged from 30 to 100 mN, and the loading, dwelling, and unloading times were all set at 10 s. Multiple indentation tests (30–80) were performed at each load for each mineral. The distance between adjacent indentations in a given specimen was at least several times the size of the indentation, to prevent interaction between the different indentations.

3.5. Load–displacement curves

The load–displacement curve was obtained for each test (Fig. 4). The curves are similar to those reported previously for various ceramics (e.g., Oliver and Pharr, 1992). The term U_3 was calculated by integrating the load–displacement data recorded 10 times per second during the indentation test. The Dx data recorded during the dwell time (10 seconds) were 5% of D_3 at maximum and were generally <3% of D_3 (Table 2).

'insert Fig. 4 and Table 2 here'

3.6 Indentations

Photomicrographs of the resulting indentations were taken with an optical microscope (Fig. 5). The indentations were only accompanied by fractures in the case of apatite at >60 mN, apophyllite at 100 mN, and gypsum at 30–100 mN. Fluorite and forsterite exhibit regular triangular indentations, while the indentation edges in the other minerals are convex toward the center of the indentations.

'insert Fig. 5'

3.7. Meyer hardness

As the standard for nanoindentation tests, we present the Meyer hardness data of the minerals obtained in our tests. The Meyer hardness (H_M) is calculated as follows:

$$H_M = \frac{P_{\max}}{A}, \qquad (18)$$

where $P_{\max}$ is the maximum load and A is the area of the residual indentation, calculated as follows:

$$A = \frac{\sqrt{3}}{4} a^2, \qquad (19)$$

where a is the apical length of the triangular residual indentation as measured on the specimen surface under a microscope. Nine measurements of a were performed for each mineral. The results at $P_{\max} = 100$ or 50 mN are listed in Table 1. These values are largely similar to published data (Broz et al., 2006).

3.8. Empirical indentation–energy rule

Table 2 summarises the measured data (Dx, D_3, and U_3) and the values calculated using equations (16) and (17) (D_r and U_r), while Fig. 6 shows the results in log D_r–log U_r space.

The log D_r and log U_r data of each mineral at various $P_{\max}$ (Fig. 6a) appear to define a straight regression line. The slope of the regression line for most of the minerals is between 2.5 and 2.9, although the slope for talc is 2.2. As the slopes are largely similar for the minerals except for talc, the regression lines appear to be almost parallel to each other. Larger values of $P_{\max}$ result in larger values of D_r and U_r on each line. The corundum line (the mineral with the highest Mohs hardness among the tested minerals) lies at the far left in Fig. 6a, while the talc line (the mineral with the lowest Mohs hardness) lies at far right. Thus, roughly speaking, the trend lines for minerals with higher Mohs hardness are located to the

left in $\log D_r$–$\log U_r$ space. However, the mineral lines are not always arranged systematically in accordance with Mohs hardness. For example, the fluorite line (Mohs hardness of 4) is to the right of the calcite line (Mohs hardness of 3), whereas the regression lines of four minerals with Mohs hardness values of 6.5–7.5 (orthoclase, forsterite, quartz, and tourmaline) are located close to each other.

Data obtained using the same $P_{\max}$ for different minerals also yield straight regression lines (Fig. 6b). The slopes of these "iso-load" lines are 1.1–1.2 (Table 3); thus, they are sub-parallel to each other. Most of the data points plot on the iso-load lines, although those for quartz and orthoclase plot slightly below the corresponding lines.

'insert Fig. 6 and Table 3 here'

3.9. Loading and unloading exponent m of analysed minerals

The loading and unloading exponent m cannot be deduced from the loading and unloading data obtained during the test, because these data include an unknown elastic deformation of the tester itself. Equation (15) indicates that the slope of the $\log D_r$–$\log U_r$ line for each mineral is equivalent to $m+1$. Thus, the value of m can be graphically determined from the slopes of the regression lines for the actual data points of each mineral, as shown in Fig. 5 and listed in Table 1. The m-values of most minerals range from 1.5 to 1.9, although the value for talc is 1.2. Although the physical meaning of the m-value is not well understood, it may relate to the elastic–plastic properties of minerals.

4. Discussion

4.1. Avoiding complex manipulation during data acquisition

Fischer-Cripps' (2006) critical review of the analysis and interpretation of instrumented indentation test data indicates that data acquisition from indentation tests is more complex and difficult than generally conceived, as highlighted by the indentation size effect (where smaller indentations indicate greater hardness). Bull (2003) and Pharr *et al*.

(2010) reviewed the indentation size effect and its various mechanisms, and demonstrated that the problem has yet to be remedied. Our experiences in data acquisition indicate that the following two issues are most troublesome: (1) evaluation of the elastic deformation of the test system under the applied load, and (2) accurate measurement of the projected area of residual indentations in specimens.

The first issue is related to the total compliance of the test system. Fischer-Cripps (2006), explaining the complexity (difficulty) that affects an exact evaluation of the compliance of the test system, emphasised the importance of compliance caused by the specimen mounting, as many researchers are unaware of this issue (p. 4160, Fischer-Cripps, 2006). In fact, in the present study we used epoxy resin to glue the specimens of quartz and calcite to the slide glasses, and set them on the specimen stage of the tester for the tests. Thus, the displacement data of quartz and calcite additionally include the elastic deformation of the epoxy resin, which was not evaluated. The complexity identified in the second issue lies in the three-dimensional curvature of the edges of the residual pyramidal indentations. It is difficult for us to precisely judge the position of the edges when quantifying the size of the indentation to calculate its projected area under optical, laser, and even atomic force microscopes.

We successfully avoided the above two issues by employing the loop energy (U_r) of Sakai (1993) in our analysis.

4.2. Advantages of the log D_r–log U_r diagram in hardness analysis

As the hardness data of most of the minerals analysed in this study have been reported previously (e.g., Szymański & Szymański, 1989; Broz *et al*., 2006; Whitney *et al*., 2007), we do not need to supply additional hardness data, thereby avoiding the second of the issues mentioned above (i.e., measuring the projected areas of the residual indentations of the specimen). Instead, we present two advantages of the log D_r–log U_r diagram.

The first advantage is estimation of m**.** We presented a method of reliably estimating the m value without evaluating the compliance of the test system. As the slope of the regression line on the log D_r–log U_r diagram is equivalent to m+1, the m value of

each mineral can be reliably determined from the diagram once the log D_r–log U_r data of instrumented indentation tests are plotted. Our m values for minerals lie within the range of values reported previously for various materials (1.2–1.9; e.g., Fischer-Cripps, 2006). The second advantage is predictability of D_r and U_r. Figure 6 is a simple graphical presentation of the relation between D_r and U_r as a function of $P_{\max}$ for various minerals. If we can obtain one pair of $D_r - U_r$ data for a mineral, then we can predict D_r when $P_{\max}$ is given and we can predict the way in which U_r increases with increasing D_r for the mineral. Even in the absence of $D_r - U_r$ data, we can roughly deduce the $D_r - U_r$ relation if the Mohs hardness of the mineral is known.

4.3. A new hardness index

As the hardness of materials usually increases with decreasing indentation size, which is referred to as indentation size effect, it seems unsatisfactory to use a single hardness number to characterise the hardness of materials, especially for indentation depths of <1 μm (e.g., Knoop *et al*., 1939; Mott, 1956; Upit & Varchenya, 1973; Nix & Gao, 1998; Pharr *et al*., 2010; Milman *et al*., 2011).

It appears necessary to present the hardness at a fixed depth when comparing the hardness of various materials (e.g., Milman *et al*., 2011). Milman *et al*. (2011) proposed depths of 0.1 μm for harder materials and 1 μm for softer materials, based on data of 21 tested ceramics and metals such as BeO, Si_3N_4, Mo, and Al. The $D_r - U_r$ diagram solves this problem by providing a new index for the hardness of minerals in terms of energy. Figure 7 shows a schematic log D_r–log U_r diagram for a mineral M. The U_r datum at D_r=1 (μm), for instance, is designated U_M following Milman *et al*. (2011). The term U_M represents the energy required to produce a 1 μm deep indentation. Table 1 provides tentative U_M data obtained at D_r=1 μm for minerals with Mohs hardness of <4.5, and data obtained at D_r=0.1 μm for minerals with Mohs hardness of >4.5. This energy-related hardness index may be useful for the energetic analysis of plastic–elastic properties (e.g., Sakai, 1999; Fischer-Cripps, 2004, p.58) and is only made possible by the development of load- and depth–sensing indentation technology.

'insert Fig. 7 here'

4.4. What is U_r?

The term U_r may be misunderstood as the energy consumed only for plastic deformation of the test specimen. This is not true, because most minerals show evidence of more-or-less elastic deformation after complete unloading, such as sink-in and protrusion along the margins of indentations. Masuda *et al*. (2011) showed that a residual stress of ~2 GPa remains around a triangular indentation in quartz after complete unloading at a load of 500 mN; hence, the amount of elastic energy is not negligible. The loop energy U_r is considered the sum of energy consumed during plastic deformation plus the energy related to elastic deformation still stored in the crystalline lattice around the site of indentation, as proposed by Sakai (1999). The separation of plastic energy from elastic energy may be the next target in seeking to obtain a quantitative understanding of deformation during indentation tests.

Acknowledgments

The authors thank Mototsugu Sakai for encouraging this study, Nozomi Kimura for critical discussions, Hideki Mori for help with sample preparation, and Sayuri Miyagishima for operating RIDER II and logistical support. The authors also thank Yuli Milman for constructive suggestions and Ian Alsop for kind comments. This study was financially supported by the Japanese Society for the Promotion of Science (16340152 to TM).

References

Brace, W., 1963. Behavior of quartz during indentation. Journal of Geology 71, 585–595.

Brace, W., 1964. Indentation hardness of minerals and rocks. Neues Jahrbuch für Mineralogie Monatshefte 9–11, 257–260.

Broz, M. E., Cook, R. F., Whitney, D. L., 2006. Microhardness, toughness and modulus of Mohs scale minerals. American Mineralogist 91, 135–142.

Bull, S. J., 2003. On the origins and mechanisms of the indentation size effect. Zeitschrift für Metallkunde 94, 787–792.

Cheng, Y.-T., Cheng, C.-M., 1998a. Relationships between hardness, elastic modulus, and the work of indentation. Applied Physics Letters 73, 614–616.

Cheng, Y.-T., Cheng, C.-M., 1998b. Scaling approach to conical indentation in elastic-plastic solids with work hardening. Journal of Applied Physics 84, 1284–1291.

Cook, R. F., Pharr, W. C., 1994. Indentation loading-displacement behaviour during conventional hardness testing. Journal of Hard Materials 5, 179–190.

Darot, M., Gueguen, Y., Benchemam, Z., Gaboriaud, R., 1985. Ductile-brittle transition investigated by micro-indentation: results for quartz and olivine. Physics of the Earth and Planetary Interiors 40, 180–186.

Dhar, P. R., Bamzai, K., Kotru, P. N., 1997. Deformation and microhardness studies on natural apophyllite crystal. Crystal Research and Technology 32, 537–544.

Doerner, M. F., Nix, W. D., 1986. A method for interpreting the data from depth-sensing indentation instruments. Journal of Materials Research 1, 601–609.

Dorner, D., Stöckhert, B., 2004. Plastic flow strength of jadeite and diopside investigated by microindentation hardness test. Tectonophysics 379, 227–238.

Evans, B., 1984. The effect of temperature and impurity content on indentation hardness of quartz. Journal of Geophysical Research 89, 4213–4222.

Evans, B., Goetze, C., 1979. Temperature variation of hardness of olivine and its implication for polycrystalline yield stress. Journal of Geophysical Research 84, 5505–5524.

Ferguson, C.C., Lloyd, G.E., Knipe, R.J., 1987. Fracture mechanics and deformation processes in natural quartz: a combined Vickers indentation, SEM and TEM study. Canadian Journal of Earth Sciences 24, 544–555.

Fischer-Cripps, A.C., 2004. Nanoindentation. Springer, Berlin.

Fischer-Cripps, A.C., 2006. Critical review of analysis and interpretation of nanoindentation test data. Surface and Coatings Technology 200, 4153–4165.

Golsby, D.L., Rar, A., Pharr, G.M., Tullis, T.E., 2004. Nanoindentation creep of quartz, with implications for rate- and state-variable friction laws relevant to earthquake mechanics. Journal of Materials Research 19, 357–365.

Grigorovich, V. K., 1976. Hardness and Microhardness of Metals. Nauka, Moscow. (cited in Milman et al., 2914)

Hodge, H.C., McKay, J.H., 1934. The “microhardness” of minerals comprising the Mohs scale. American Mineralogist 19, 161–168.

Karato, S., Ito, E., Fujino, K., 1990. Plasticity of $MgSiO_3$ perovskite: the results of microhardness tests on single crystals. Geophysical Research Letters 17, 13–16.

Karato, S., Wang, Z.C., Liu, B., Fujino, K., 1986. Plastic deformation of garnets: Systematics and implications for the rheology of the mantle transition zone. Earth and Planetary Science Letters 130, 13–30.

Knoop, F., Peters, C.G., Emerson, W.B., 1939. A sensitive pyramidal-diamond tool for indentation measurements. Journal of Research of the National Bureau of Standards 23, 39–61.

Li, H., Bradt, R.C., 1990. Knoop microhardness anisotropy of single-crystal rutile. Journal of American Ceramic Society 73, 1360–1364.

Li, H., Bradt, R.C., 1991. Knoop microhardness anisotropy of single-crystal cassiterite (SnO_2). Journal of American Ceramic Society 74, 1053–1060.

Masuda, T., Hiraga, T., Ikei, H., Kanda, H., Kugimiya, Y., Akizuki, M., 2000. Plastic deformation of quartz at room temperature: a Vickers nano-indentation test. Geophysical Research Letters 27, 2773–2776.

Masuda, T., Miyake, T., Enami, M., 2011. Ultra-high residual compressive stress (>2 GPa) in a very small volume (<1 μm^3) of indented quartz. American Mineralogist 96, 283–287.

Milman, Yu.V., Golubenko, A.A., Dub, S.N., 2011. Indentation size effect in nanohardness. Acta Materialia 59, 7480–7487.

Milman, Yu.V., Grinkevich, K.E., Mordel, L.V., 2014. Energy concept of hardness for instrumented indentation. Russian Metallurgy (Metally), 2014, 256–262.

Mott, B.W., 1956. Micro-Indentation Hardness Testing. Butterworths Scientific Publications, London.

Nix, W.D., Gao, H., 1998. Indentation size effects in crystalline materials: a law for strain gradient plasticity. Journal of the Mechanics and Physics of Solids 46, 411–425.

Nowak, R., Sakai, M., 1994. The anisotropy of surface deformation of sapphire: continuous indentation of triangular indenter. Acta Metallurgica et Materialia 42, 2879–2891.

Oliver, W.C., Pharr, G.M., 1992. An improved technique for determining hardness and elastic modulus using load and displacement sensing indentation experiments. Journal of Materials Research 7, 1564–1583.

Pethica, J.B., Huchings, R., Oliver, W.C., 1983. Hardness measurement at depth as small as 20 nm. Philosophical Magazine, Series A 48, 593–606.

Pharr, G.M., Herbert, E.G., Gao, Y., 2010. The indentation size effect: a critical examination of experimental observations and mechanistic interpretations. Annual Review of Materials Research 40, 271–292.

Sakai, M., 1993. Energy principle of the indentation-induced inelastic surface deformation and hardness of brittle materials. Acta Metallurgica et Materialia 41, 1751–1758.

Sakai, M., 1999. The Meyer hardness: A measure for plasticity? Journal of Materials Research 14, 3630–3639.

Sakai, M., Shimizu, S., Ishikawa, T., 1999. The indentation load-depth curve of ceramics. Journal of Materials Research 14, 1471–1484.

Szymański, A., Szymański, J.M., 1989. Hardness Estimation of Minerals, Rocks and Ceramic Materials. Materials Science Monographs 49, Elsevier, Amsterdam.

Tabor, D., 1951. The Hardness of Metals. Oxford University Press, Oxford.

Tabor, D., 1954. Mohs's hardness scale – A physical interpretation. Proceedings of the Physical Society, Section B 67, 249–257.

Tabor, D., 1996. Indentation hardness: fifty years on. Philosophical Magazine, Series A, 74, 1207–1212.

Upit, G.P., Varchenya, S.S., 1973. The size effect in the hardness of single crystals. In: J.H. Westbrook, J.H., Conrad, H. (eds.), The Science of Hardness Testing and its Research Applications. American Society for Metals, Metals Park, Ohio, pp. 135–146.

Walley, S.M., 2012. Historical origins of indentation hardness testing. Materials Science and Technology 28, 1028–1044.

Westbrook, J.H., 1958. Temperature dependence of strength and brittleness of some quartz structures. Journal of the American Ceramic Society 41, 433–440.

Westbrook, J.H., Conrad, H., 1973. The Science of Hardness Testing and its Research Applications. American Society for Metals, Metals Park, Ohio.

Whitney, D.L., Broz, M., Cook, R.F., 2007. Hardness, toughness, and modulus of some common metamorphic minerals. American Mineralogist 92, 281–288.

Winchell, H., 1945. The Knoop microhardness tester as a mineralogical tool. American Mineralogist 30, 583–595.

Table and figure captions

Table 1. Description of mineral samples and list of m values.

Table 2. Data (Δx, D_3, U_3, D_r, and U_r) obtained from the indentation tests.

Table 3. Obtained slope at each $P_{\max}$ value in the $\log D_r$–$\log U_r$ diagram.

Fig. 1. Schematic ideal relation between the load (x) and penetration depth (y) of the indenter into the specimen. The shaded area is loop energy (U_r), which represents the energy consumed to produce an indentation of depth D_r.

Fig. 2. Schematic load–displacement curve for actual indentation tests. Three displacement variables (D_1, D_2, and D_3) are measured by the tester. Note that displacement is not equal to the penetration depth, because the loading and unloading curves are influenced by elastic deformation of the tester (dashed line), and this has yet to be evaluated in detail. The values of D_3, Δx, and U_3 are not influenced by elastic deformation of the tester. The length Δx is exaggerated in the figure.

Fig. 3. Photographs of the specimens. Dots and lines drawn on the surfaces of the specimens were used for focusing under the indentation tester. Scale bar = 1 cm. (a) Corundum, (b) topaz, (c) tourmaline, (d) quartz, (e) forsterite, (f) orthoclase, (g) apatite, (h) apophyllite, (i) fluorite, (j) gypsum, (k) calcite, and (l) talc. The apatite and talc specimens are polycrystalline; the others are single crystals.

Fig. 4. Typical load–displacement curves of the tested minerals. The curves for talc and gypsum appear to be unstable. Such weak minerals (the Mohs hardness values of talc and gypsum are 1 and 2, respectively) always show such instabilities. We cannot

estimate the m values from these curves because measured displacement is not equivalent to the penetration depth.

Fig. 5. Photomicrographs of indentations in (a) corundum (maximum load of 100 mN), (b) topaz (100 mN), (c) tourmaline (100 mN), (d) quartz (100 mN), (e) forsterite (100 mN), (f) orthoclase (100 mN), (g) apatite (100 mN), (h) apophyllite (50 mN), (i) fluorite (50 mN), (j) calcite (50 mN), (k) gypsum (50 mN), and (l) talc (50 mN). The indentations in orthoclase are circled to aid viewing (f). Scale bar = 50 μm.

Fig. 6. log D_r–log U_r diagrams for the analysed mineral specimens. Each data point represents the arithmetic mean of 30–80 tests, and the error bars are one standard deviation. (a) Data points of each mineral under various loads are arranged on each "mineral line" that yield correlation coefficients of >0.99 for the fitting. (b) Data points of various minerals for a given $P_{\max}$ are arranged on "iso-load lines" that yield correlation coefficients of >0.99. The top line shows data for $P_{\max}$ = 100 mN, while the bottom line shows data for $P_{\max}$ = 30 mN. The lines correspond to $P_{\max}$ values at intervals of 10 mN. The slopes of all the lines are between 1.1 and 1.2. In both diagrams, the data of forsterite are plotted but are concealed behind the data points of quartz, orthoclase, and tourmaline. The forsterite data can be viewed in Table 2.

Fig. 7. Schematic diagram showing the index U_M for a given mineral M. As an example, U_M is designated as the value of U_r at D_r = 1 μm.

Mineral	Mohs hardness scale	Where from?	ngle crystallin	Thickness (mm)	m value	U_M(nJ) at D_r=0.1 mr	U_M(nJ) at D_r=1 mm	Meyer hardness (GPa)	
Talc	1	Austria	Polycrystalline	7	1.2	0.096	14	0.5 ± 0.07	#2
Gypsum	2	Mexico	ingle crystallin	5	1.4	0.085	27	1.7 ± 0.25	#2
Calcite	3	USA	ingle crystallin	1*	1.9	0.068	51	2.2 ± 0.15	#2
Fluorite	4	Spain	ingle crystallin	6	1.5	0.035	37	2.1 ± 0.07	#2
Apophyllite	4.5	India	ingle crystallin	6	1.5	0.27	84	4.6 ± 0.36	#2
Apatite	5	Madagascar	Polycrystalline	6	1.6	0.32	120	7.0 ± 0.49	#1
Orthoclase	6	China	ingle crystallin	3	1.9	0.42	330	9.3 ± 1.5	#1
Forsterite	6.5	Pakistan	ingle crystallin	5	1.8	0.47	300	15 ± 1.4	#1
Quartz	7	Brazil	ingle crystallin	1*	1.6	0.55	230	14 ± 0.84	#1
Tourmaline	7.5	?	ingle crystallin	4	1.7	0.51	270	13 ± 0.72	#1
Topaz	8	Brazil	ingle crystallin	6	1.7	0.89	490	23 ± 1.6	#1
Corundum	9	?	ingle crystallin	5	1.6	1.3	500	27 ± 3.5	#1

* Glued to slide grass with epoxy resin
#1: maximum load =100 mN, #2: maximum load = 50 mN

	P_{max}	Corundum	Topaz	Tourmaline	Quartz	Forsterite	Orthoclase	Apatite	Apophyllite	Fluorite	Calcite	Gypsum	Talc
Δx (nm)	100	6 ± 1	5 ± 1	7 ± 2	1 ± 2	6 ± 2	3 ± 2	12 ± 2	23 ± 4	103 ± 2	63 ± 4	32 ± 18	110 ± 48
	90	6 ± 2	5 ± 2	8 ± 2	2 ± 1	7 ± 1	8 ± 2	9 ± 2	21 ± 3	98 ± 2	57 ± 4	35 ± 16	94 ± 28
	80	5 ± 1	6 ± 2	8 ± 1	5 ± 1	8 ± 2	9 ± 1	11 ± 1	19 ± 2	95 ± 2	55 ± 5	29 ± 10	103 ± 33
	70	4 ± 2	1 ± 1	5 ± 1	5 ± 1	8 ± 1	8 ± 1	9 ± 2	14 ± 3	90 ± 1	53 ± 4	32 ± 18	88 ± 37
	60	5 ± 1	4 ± 1	10 ± 2	0 ± 1	8 ± 2	5 ± 2	10 ± 2	15 ± 2	83 ± 1	47 ± 3	27 ± 10	84 ± 39
	50	1 ± 1	1 ± 1	6 ± 1	3 ± 2	7 ± 1	5 ± 1	7 ± 2	14 ± 2	73 ± 2	44 ± 3	30 ± 17	62 ± 14
	40	4 ± 2	5 ± 2	9 ± 2	5 ± 2	6 ± 1	5 ± 1	5 ± 1	10 ± 3	69 ± 1	39 ± 3	26 ± 17	64 ± 26
	30	3 ± 2	3 ± 2	5 ± 1	3 ± 2	6 ± 1	4 ± 1	4 ± 1	13 ± 2	58 ± 1	34 ± 2	23 ± 13	47 ± 21
D_3 (nm)	100	188 ± 12	232 ± 17	306 ± 9	244 ± 9	304 ± 11	273 ± 22	466 ± 16	544 ± 42	1085 ± 26	960 ± 17	1288 ± 89	2870 ± 400
	90	183 ± 12	215 ± 11	285 ± 13	238 ± 10	296 ± 24	266 ± 24	433 ± 30	536 ± 36	1022 ± 18	867 ± 17	1192 ± 49	2515 ± 413
	80	161 ± 7	196 ± 11	274 ± 12	226 ± 8	278 ± 10	263 ± 22	417 ± 35	485 ± 38	964 ± 12	829 ± 23	1136 ± 95	2321 ± 416
	70	149 ± 11	173 ± 12	249 ± 7	214 ± 5	254 ± 8	239 ± 17	377 ± 11	439 ± 37	909 ± 16	810 ± 14	1013 ± 67	2074 ± 295
	60	136 ± 7	167 ± 10	233 ± 11	175 ± 6	232 ± 7	224 ± 15	352 ± 12	409 ± 42	837 ± 12	713 ± 21	969 ± 48	1974 ± 387
	50	114 ± 10	141 ± 12	207 ± 6	164 ± 8	214 ± 8	203 ± 15	304 ± 23	376 ± 29	724 ± 17	661 ± 15	815 ± 59	1646 ± 210
	40	108 ± 7	133 ± 8	185 ± 11	151 ± 7	187 ± 14	173 ± 11	268 ± 11	308 ± 34	644 ± 13	578 ± 13	749 ± 57	1346 ± 265
	30	90 ± 7	114 ± 6	157 ± 6	125 ± 7	156 ± 6	145 ± 12	222 ± 10	265 ± 33	539 ± 13	503 ± 14	579 ± 40	1050 ± 229
U_3 (nJ)	100	6.59 ± 0.29	8.03 ± 0.27	10.9 ± 0.4	6.10 ± 0.24	10.8 ± 0.3	8.26 ± 0.92	17.7 ± 0.7	20.1 ± 1.5	47.3 ± 0.4	41.6 ± 0.6	50.60 ± 5.09	131.8 ± 22.3
	90	6.01 ± 0.49	6.89 ± 0.36	9.24 ± 0.58	5.59 ± 0.16	9.47 ± 0.26	7.55 ± 0.66	14.9 ± 0.7	17.4 ± 1.0	40.1 ± 0.4	35.1 ± 0.5	40.70 ± 2.89	101.5 ± 18.8
	80	4.57 ± 0.17	5.77 ± 0.32	7.75 ± 0.24	4.88 ± 0.15	8.09 ± 0.29	6.65 ± 0.59	12.4 ± 0.8	14.4 ± 1.1	33.9 ± 0.3	29.5 ± 0.7	36.30 ± 2.93	92.8 ± 14.0
	70	3.49 ± 0.21	3.92 ± 0.19	5.97 ± 0.18	4.01 ± 0.08	6.55 ± 0.17	5.16 ± 0.43	9.89 ± 0.25	11.0 ± 0.9	28.0 ± 0.2	24.6 ± 0.4	28.60 ± 2.07	73.5 ± 11.2
	60	2.91 ± 0.20	3.60 ± 0.16	5.48 ± 0.31	2.56 ± 0.13	5.00 ± 0.10	3.96 ± 0.49	7.96 ± 0.19	8.30 ± 0.82	22.1 ± 0.1	19.2 ± 0.4	22.8 ± 1.9	53.0 ± 12.0
	50	1.87 ± 0.14	2.36 ± 0.12	3.64 ± 0.11	2.17 ± 0.15	3.80 ± 0.11	2.97 ± 0.35	5.78 ± 0.36	6.81 ± 0.53	16.4 ± 0.3	14.5 ± 0.2	16.9 ± 1.8	36.0 ± 5.8
	40	1.54 ± 0.14	1.93 ± 0.07	3.00 ± 0.20	1.66 ± 0.05	2.66 ± 0.07	2.04 ± 0.22	4.00 ± 0.11	4.62 ± 0.53	12.1 ± 0.1	10.4 ± 0.2	11.8 ± 0.7	25.3 ± 3.9
	30	0.94 ± 0.08	1.16 ± 0.09	1.67 ± 0.04	1.04 ± 0.07	1.69 ± 0.06	1.33 ± 0.15	2.51 ± 0.08	3.16 ± 0.31	7.72 ± 0.06	6.64 ± 0.17	7.33 ± 0.56	15.9 ± 3.6
D_r (nm)	100	182 ± 12	227 ± 16	299 ± 8	243 ± 8	298 ± 10	270 ± 21	454 ± 15	521 ± 41	981 ± 25	897 ± 16	1256 ± 86	2760 ± 386
	90	177 ± 10	210 ± 10	276 ± 11	236 ± 9	286 ± 10	258 ± 23	428 ± 16	515 ± 35	924 ± 18	810 ± 16	1157 ± 51	2422 ± 392
	80	156 ± 7	190 ± 11	265 ± 8	221 ± 8	270 ± 9	254 ± 21	411 ± 19	466 ± 37	869 ± 12	774 ± 20	1107 ± 96	2219 ± 401
	70	145 ± 10	173 ± 11	244 ± 7	209 ± 6	247 ± 8	231 ± 16	373 ± 36	424 ± 36	819 ± 15	757 ± 13	975 ± 73	1986 ± 287
	60	131 ± 6	162 ± 10	223 ± 10	175 ± 6	224 ± 7	220 ± 14	342 ± 11	394 ± 41	754 ± 12	665 ± 21	942 ± 45	1881 ± 373
	50	113 ± 10	140 ± 11	201 ± 5	161 ± 7	207 ± 8	197 ± 15	297 ± 22	363 ± 28	651 ± 18	617 ± 14	785 ± 61	1584 ± 203
	40	105 ± 7	130 ± 10	177 ± 10	146 ± 7	180 ± 8	168 ± 11	263 ± 11	297 ± 32	576 ± 13	540 ± 14	722 ± 57	1282 ± 257
	30	87 ± 5	110 ± 5	152 ± 6	122 ± 7	151 ± 5	140 ± 11	218 ± 10	252 ± 32	480 ± 13	469 ± 13	556 ± 41	1002 ± 214
U_r (nJ)	100	6.00 ± 0.26	7.50 ± 0.20	10.2 ± 0.4	5.97 ± 0.14	10.2 ± 0.2	7.98 ± 0.78	16.5 ± 0.6	17.9 ± 1.3	36.9 ± 0.3	35.4 ± 0.5	47.42 ± 4.83	120.8 ± 20.2
	90	5.44 ± 0.32	6.45 ± 0.25	8.51 ± 0.41	5.37 ± 0.15	8.84 ± 0.21	6.85 ± 0.56	14.0 ± 0.5	15.5 ± 0.9	31.3 ± 0.3	29.9 ± 0.5	37.74 ± 2.93	93.0 ± 17.4
	80	4.18 ± 0.16	5.32 ± 0.22	7.12 ± 0.19	4.47 ± 0.11	7.49 ± 0.21	5.95 ± 0.51	11.7 ± 0.3	12.8 ± 1.0	26.4 ± 0.2	25.1 ± 0.6	34.11 ± 3.19	84.6 ± 12.7
	70	3.24 ± 0.14	3.88 ± 0.14	5.64 ± 0.13	3.66 ± 0.09	6.03 ± 0.14	4.61 ± 0.38	9.24 ± 0.19	9.96 ± 0.79	21.7 ± 0.2	20.9 ± 0.4	26.4 ± 2.1	67.3 ± 10.7
	60	2.64 ± 0.13	3.34 ± 0.13	4.89 ± 0.27	2.54 ± 0.13	4.54 ± 0.11	3.68 ± 0.40	7.39 ± 0.15	7.93 ± 0.76	17.1 ± 0.1	16.3 ± 0.4	21.3 ± 2.0	48.0 ± 10.8
	50	1.82 ± 0.12	2.32 ± 0.09	3.36 ± 0.08	2.02 ± 0.09	3.44 ± 0.09	2.71 ± 0.31	5.44 ± 0.31	6.12 ± 0.48	12.8 ± 0.2	12.3 ± 0.2	15.5 ± 1.9	32.9 ± 5.3
	40	1.39 ± 0.10	1.75 ± 0.05	2.65 ± 0.16	1.47 ± 0.09	2.41 ± 0.06	1.84 ± 0.19	3.81 ± 0.09	4.21 ± 0.46	9.32 ± 0.06	8.82 ± 0.22	10.8 ± 0.8	22.8 ± 3.3
	30	0.85 ± 0.05	1.06 ± 0.05	1.54 ± 0.04	0.94 ± 0.07	1.52 ± 0.04	1.20 ± 0.13	2.38 ± 0.07	2.78 ± 0.28	5.97 ± 0.04	5.62 ± 0.14	6.64 ± 0.65	14.5 ± 3.2

P_{max} (mN	30	40	50	60	70	80	90	100
slope	1.2	1.2	1.2	1.1	1.2	1.2	1.1	1.1

Fig. 1. Loop energy (parallelogram)

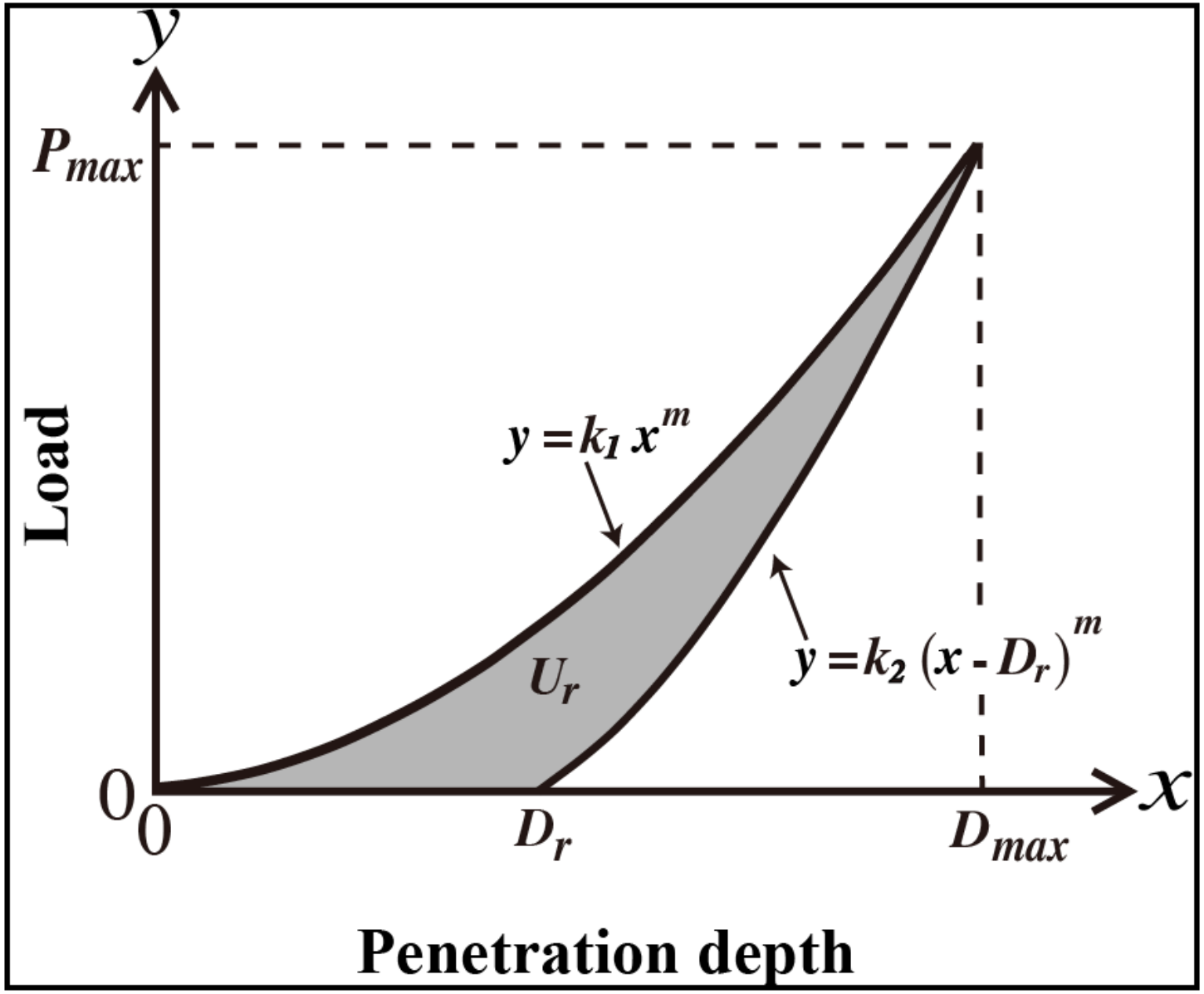

Fig. 2. Loop energy (parallelogram)

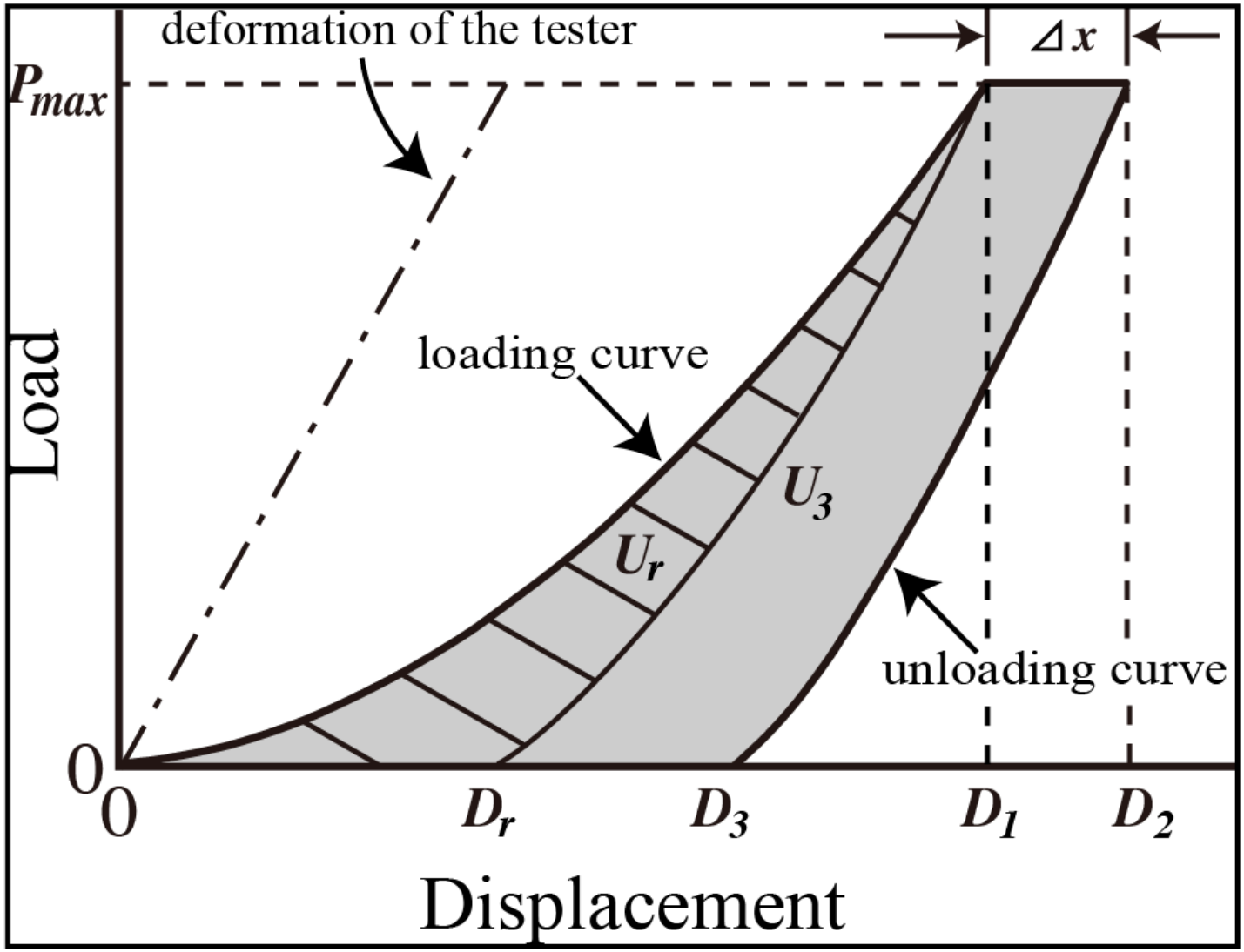

Fig. 3. Loop energy (parallelogram)

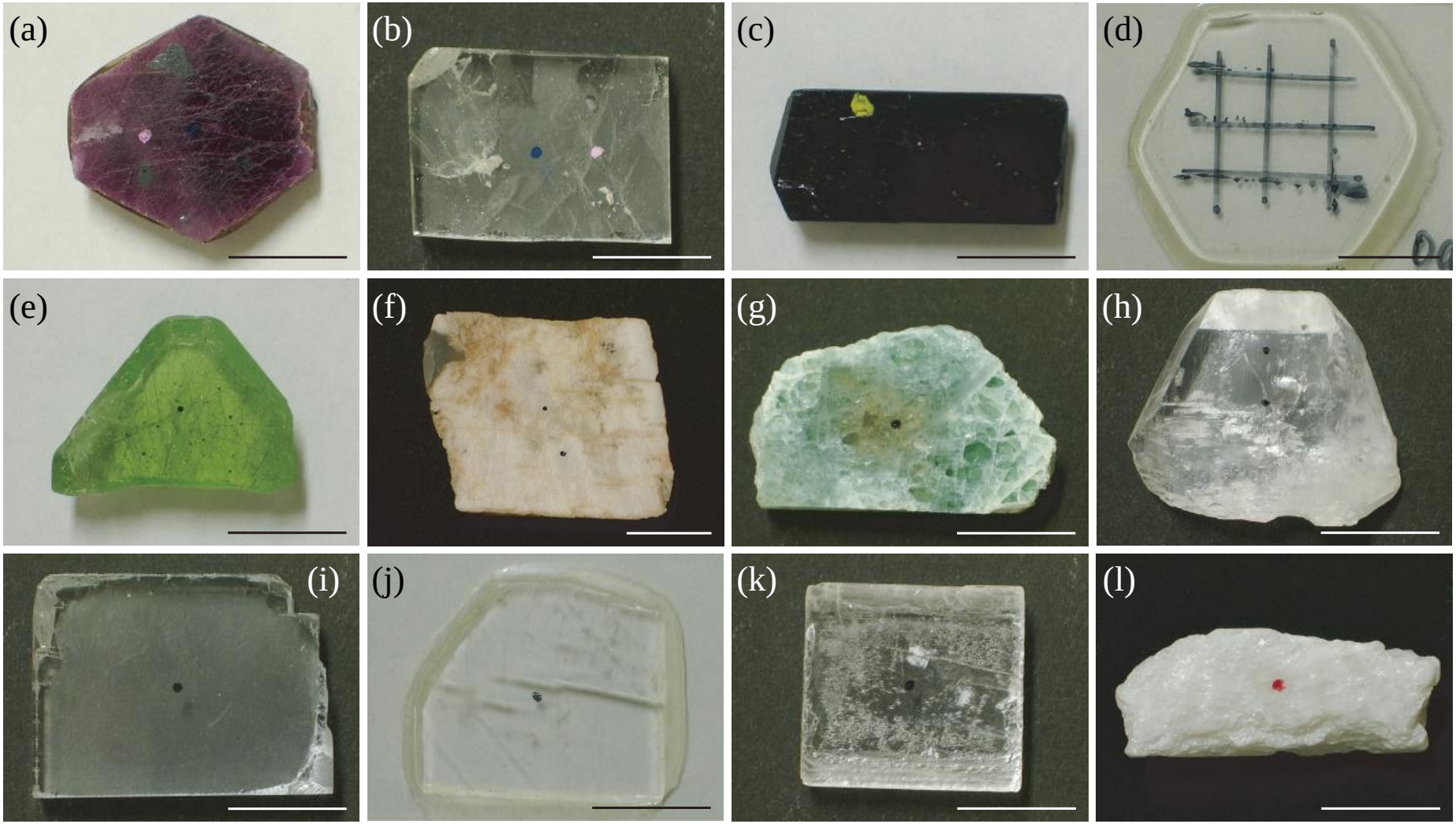

Fig. 4. Loop energy (parallelogram)

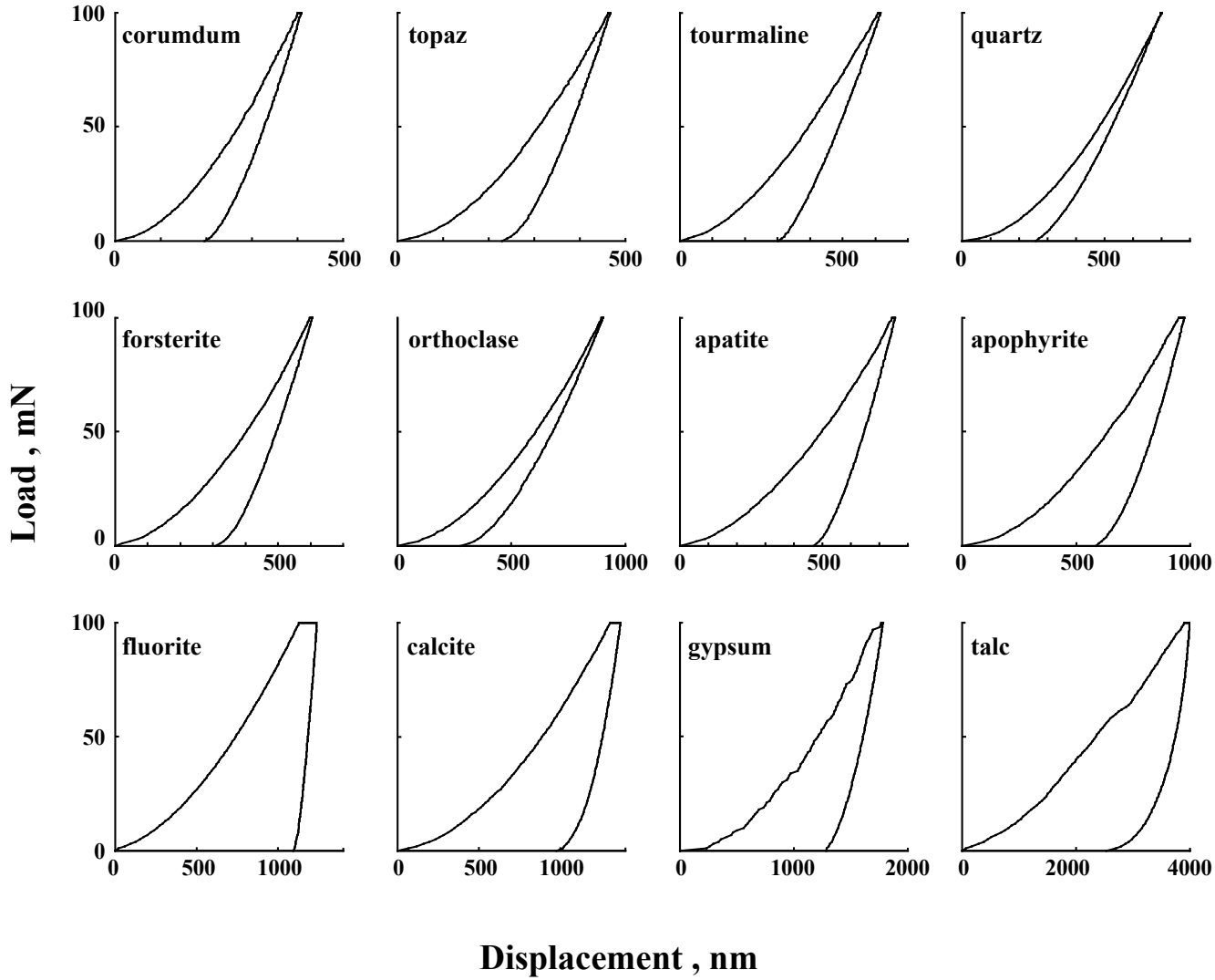

Fig. 5. Loop energy (parallelogram)

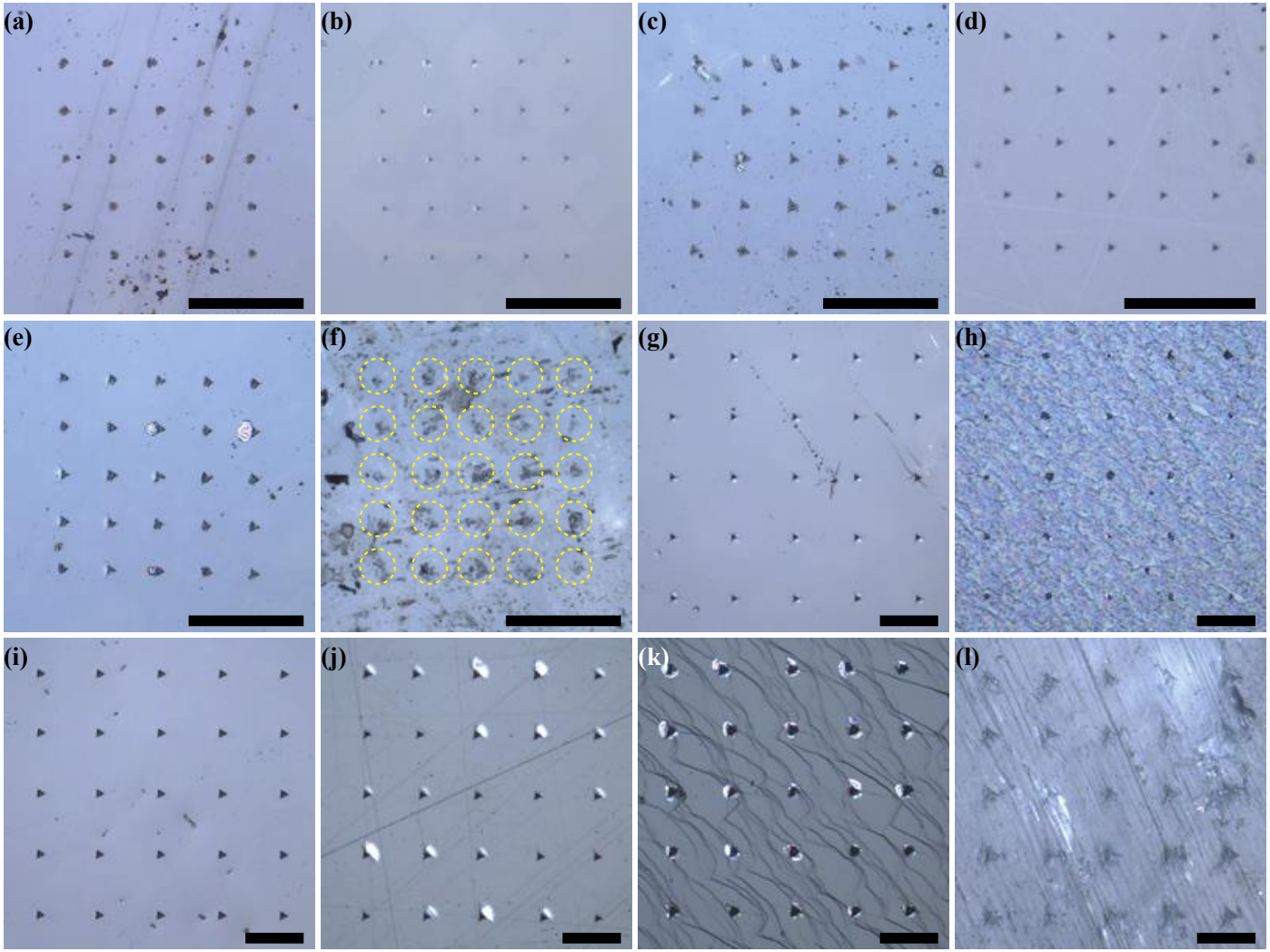

Fig. 6. Loop energy (Parallelogram)

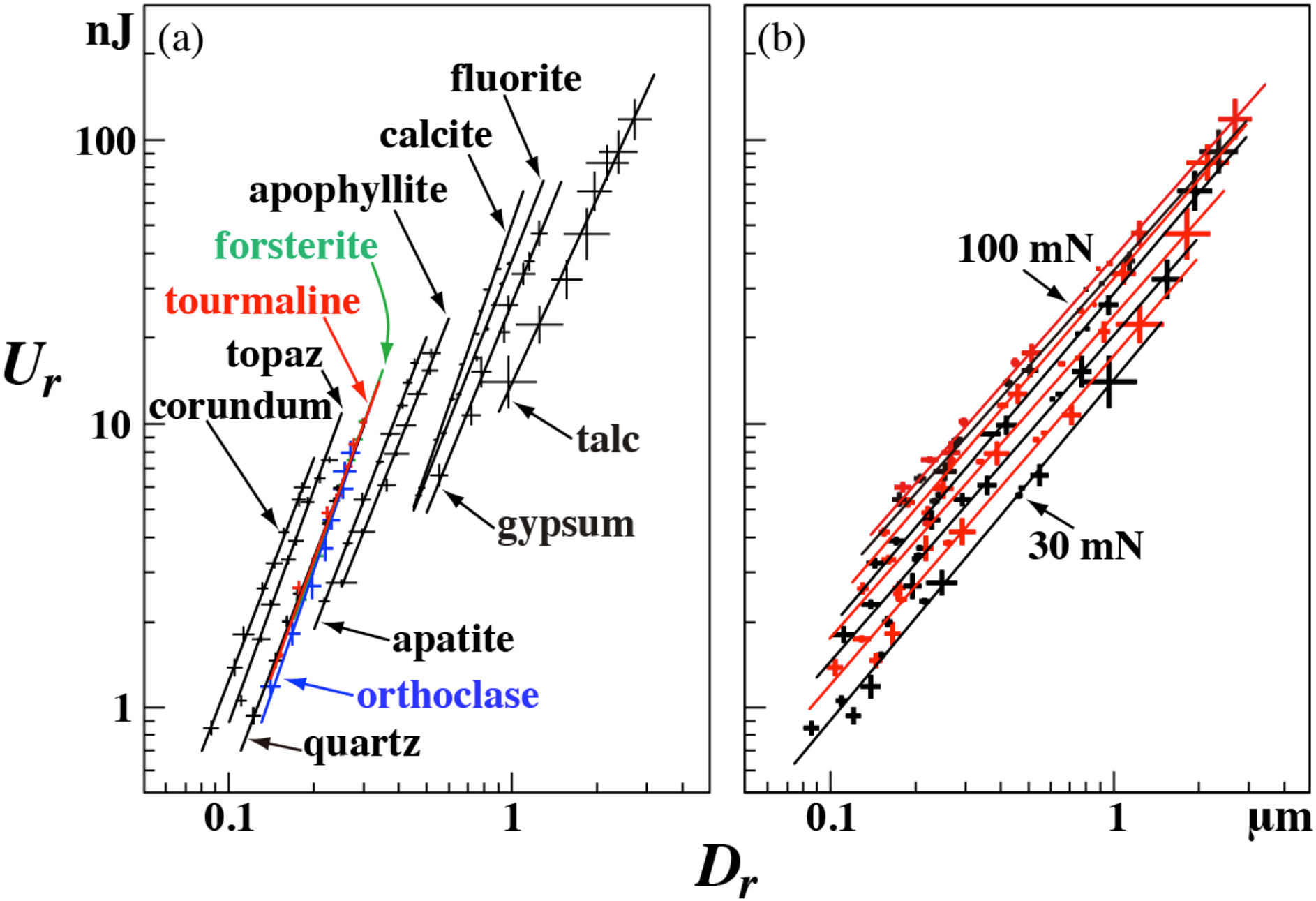

Fig. 7. Loop energy (parallelogram)